ARTICLES

Three-Dimensionally Ordered Macroporous ZrO_2:Eu^{3+}: Photonic Band Effect and Local Environments

Xuesong Qu,[†] Hongwei Song,*[,‡] Guohui Pan,[†] Xue Bai,[‡] Biao Dong,[‡] Haifeng Zhao,[†] Qilin Dai,[†] Hui Zhang,[†] Ruifei Qin,[†] and Shaozhe Lu[†]

Key Laboratory of Excited State Physics, Changchun Institute of Optics, Fine Mechanics and Physics, Chinese Academy of Sciences, and Graduate School of Chinese Academy of Sciences, 16 Eastern Nan-Hu Road, Changchun 130033, People's Republic of China, and State Key Laboratory on Integrated Optoelectronics, College of Electronic Science and Engineering, Jilin University, Changchun 130012, People's Republic of China

Received: August 22, 2008; Revised Manuscript Received: January 23, 2009

Three-dimensionally ordered macroporous (3DOM) ZrO_2:Eu^{3+} inverse opal materials prepared by polystyrene (PS) colloidal crystal templating, using the sol−gel method, were successfully fabricated. Their crystal structure, morphology, and photoluminescence (PL) properties and the effect of the photonic stop-band on the spontaneous emission of Eu^{3+} ions were studied and compared with those of the nonporous sample. In the 3DOM ZrO_2:Eu^{3+}, significant suppression for the $^5D_0$-$^7F_1$ transition peaking at 590 nm was observed, which was in good agreement with the photonic band gap calculated (∼586 nm). After grinding the 3D ZrO_2:Eu^{3+} inverse opal material, the suppression of emission was restored due to the disappearance of the photonic band gap. In the 3DOM ZrO_2:Eu^{3+}, the luminescent lifetime of $^5D_0$-^7F_J depended strongly on emission wavelengths, which was mainly attributed to the appearance of different Eu^{3+} centers. In the 3DOM ZrO_2:Eu^{3+}, three symmetry sites for Eu^{3+} were identified by site-selective excitation, differing from the nonporous sample, in which only one site was identified.

I. Introduction

Since the pioneering works by Yablonovitch[1] and John[2] in 1987, 3DOM materials, known as photonic crystals, have attracted considerable scientific and technological interest. Possessing spatial periodicity in their dielectric constant on the length scale of the optical wavelength, photonic crystals behave with respect to electromagnetic waves like atomic crystals do with respect to electrons. As an electronic band gap is created by the periodic arrangement of atoms in a semiconductor, the periodic electromagnetic modulation created by a photonic crystal can yield a photonic band gap (PBG), a band of frequencies for which light propagation in the photonic crystal is forbidden. Because of their ability to confine, control, and manipulate photons in up to 3D, PBG materials have demonstrated a wide variety of applications, for example, as optical waveguides with sharp bends, as optical circuits, as optical signal modulators, and as a tool to control the spontaneous emission of excited atoms and molecules.[3−8] Among these applications, one of such interesting physical issue is the modification of the spontaneous emission, which may serve as a basis for zero-threshold lasers.[7,8] To date, several experimental studies have been reported on formation of the macroporous photonic crystals and the modification of spontaneous emission by embedding luminescent species in the photonic crystals, including organic dyes, semiconductors, and rare earth ions.[9−15] However, in these experimental studies the luminescent species were grafted or coated on the inner surfaces of the opals/inverse opal structure. Examples such as dye molecules embedded in PS opals,[9,10] SiO_2 opals doped with Eu^{3+} ions,[11] Er^{3+} ions,[12,13] LaF_3:Tb^{3+}nanoparticles,[14] and TiO_2 inverse opals doped with CdSe nanocrystals[15] were prepared and significant suppression and enhancement of spontaneous emission have been studied. To our knowledge, a few examples of the inverse opal in the system of luminescent matrix including ZnS:Mn, Zn_2SiO_4:Mn, $LaPO_4$:Tb^{3+}, and TiO_2:Er^{3+} have been reported.[16−19]

As is well-known, the emission band of fluorescent dyes is often broader than the width of the photonic stop band and only a part of the emission spectrum could be affected by photonic crystals structure. Thus, light emitters with a narrow emission band would be an ideal choice to maximize the photonic crystal effect. Hence, rare earth ions involving f-orbital electrons with much narrower emission than the photonic stop band of typical inverse opal structures would be a tool to study the photonic crystal effect. To date, only a few experimental works of the inverse opal in the system of luminescent matrix with rare earth ions have been reported. In the present work, the Eu^{3+}-doped ZrO_2 inverse opal photonic crystals were prepared by PS colloidal crystal templating, using the sol−gel method. The PL properties and the effect of the photonic band gap structure on the emission characteristics were studied and compared with the nonporous and crushed samples. In such a system, Eu^{3+}

* To whom correspondence should be addressed. E-mail: hwsong2005@yahoo.com.cn.

† Key Laboratory of Excited State Physics, Changchun Institute of Optics, Fine Mechanics and Physics, Chinese Academy of Sciences, and Graduate School of Chinese Academy of Sciences.

‡ State Key Laboratory on Integrated Optoelectronics, College of Electronic Science and Engineering, Jilin University.

10.1021/jp8075063 CCC: $40.75
Published on Web 03/24/2009

SCHEME 1: Schematic Diagram Showing the Process for Preparation of 3DOM $ZrO_2:Eu^{3+}$ Powders by Templating Technique

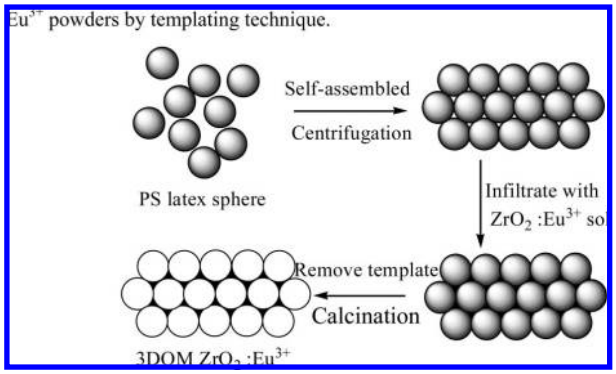

ions may act as an activator to detect the change of local environments in different samples due to the supersensitive f−f transitions. As have been studied by some articles,[20−22] local symmetry and surface effects play a very important role in the luminescence of rare earth doped nanocrystals. It is important to distinguish whether the photonic band gap or local environments lead to the changes of PL intensity and the dynamics in this kind of 3DOM material. It is expected that the Eu^{3+} ions doped nanosized PL material with 3DOM structure would offer an example to realize these two kinds of effects. In addition, ZrO_2, as an efficient luminescent host (phonon energy 470 cm^{-1}), [23−25] has a high refractive index, which may be important for PBG materials and other photonic applications.

II. Experimental Details

II.1. Sample Preparation. 3DOM $ZrO_2:Eu^{3+}$ powders were prepared by templating technique and an overview of our preparative strategy is schematically shown in Scheme 1. First, a self-assembled colloidal crystal structure was used as a prototype for 3D $ZrO_2:Eu^{3+}$ photonic crystals. The doping concentration of Eu^{3+} was 5 mol % of ZrO_2 in $ZrO_2:Eu^{3+}$. In the present work, a monodisperse PS latex sphere was synthesized and packed into a colloidal crystal by centrifugation for 24 h according to the literature by Holland et al.[26] In the preparation of a $ZrO_2:Eu^{3+}$ sol precursor, appropriate amounts of $EuCl_3$ were dissolved in ethanol under vigorous stirring, then added quickly to an ice-cooled solution of $Zr(n\text{-}OC_4H_9)_4$ followed by further stirring for 30 min. Then, the resulting mixed $ZrO_2:Eu^{3+}$ sol (2 g) was dripped on PS (1 g) spheres, which were then spread on a filter paper placed in a Büchner funnel while suction was applied. The resulting products were dried in air at room temperature for 24 h. Finally, 3DOM $ZrO_2:Eu^{3+}$ inverse opal was obtained after removal of the PS template by a thermal treatment consisting of a slow rising time of 3 h from room temperature to 500 °C and a keeping time of 5 h at 500 °C. In this paper, three different dilution ratios (the molar ratio of the reactants $Zr(n\text{-}OC_4H_9)_4$ to C_2H_5OH) 1:1,1:2, and 1:5 were chosen to prepare the samples of 5 mol % Eu^{3+} with PS (400 nm) as templates. To investigate the influence of a photonic stop band on the PL spectra of the 3DOM materials, two monodisperse PS latex spheres with different particle sizes (400 and 380 nm) were chosen as templates to obtain samples, PC1, for which the stop band overlaps with the PL emission band, and PC2, for which the band does not overlap with the PL emission band. The influence of the photonic crystal structure of $ZrO_2:Eu^{3+}$ on its PL emission spectrum was also investigated directly by grinding the sample to destroy the regular 3D order structure. For comparison, the corresponding nonporous $ZrO_2:Eu^{3+}$ sample was prepared and annealed by the same procedure without the PS colloidal templates.

II.2. Measurements and Characterization. X-ray diffraction (XRD) patterns of the samples were obtained with a Rigaku D/max-rA X-Ray diffractometer with Cu Kα radiation. Fourier-transform infrared spectra (FI-IR) were measured by a Nexus 670 FT-IR spectrophotometer. Field emission scanning electron micrograph (FESEM) images were taken on a Hitachi S-4800 electron microscope. Fluorescence and excitation were recorded on a Hitachi F-4500 spectrophotometer equipped with a 150 W Xe-arc lamp at room temperature. In the measurement of time-resolved fluorescence spectra, a 266-nm light generated from the fourth-harmonic generator pumped by the pulsed Nd:YAG laser was used as the excitation source. A line width of 1.0 cm^{-1}, pulse duration of 10 ns, and repetition frequency of 10 Hz were used. A Rhodamine 6 G dye pumped by the same Nd:YAG laser was used as the site selective excitation source. The spectra were recorded by a Spex-1403 spectrometer, a photomultiplier, and a boxcar integrator and processed by a computer. Luminescent decay curves were recorded by an oscillograph (Tektronix, TDS3052, 500 MHz, 5Gs/s), also with a 266-nm light as the excitation source.

III. Results and Discussion

III.1. Crystal Structure and Morphology. Figure 1 shows FESEM images of the PS opal (Figure 1A), 3DOM $ZrO_2:Eu^{3+}$ inverse opal (Figure 1B−H), and the crushed samples (Figure 1). From Figure 1A, monodisperse PS latex spheres exhibit an average diameter of 400 nm and they are packed in a face centered cubic (fcc) structure with (111) orientation, which is deduced from the ordered array pattern of the microspheres. In Figure 1B,C and Figure 1D−F, SEM images of PC1 and PC2 are presented, respectively. Although still containing some defects and cracks, the samples exhibit a long-range 3D ordered structure comprising interconnected macropores that form order hexagonal arrangement of air spheres, which corresponds to the (111) surface of a fcc structure. The center-to center distance between the air spheres on the (111) planes is about 285 and 260 nm for PC1 and PC2, respectively. Both samples are about 29% smaller compared with the corresponding PS templates due to the shrinkage during the process of calcinations.[26] From Figure 1F, the $ZrO_2:Eu^{3+}$ nanoparticles with a homogeneous particle size distribution (10−15 nm) aggregate on the wall and constitute the 3DOM skeleton.

The SEM images in Figure 1 (panels B−C, G, and H) depict the changes in wall thickness and ordering of the structure of the samples obtained at various dilution ratios. From the SEM images, it is suggested that the 3D parameters including the wall thickness, the center-to-center distance, and ordering of the pores of the powder were strongly related to the concentration of the precursors because the viscosity and hydrolysis/condensation rate of the precursors was affected by the concentration. When the dilution ratio was 1:1, a well-ordered macroporous structure was obtained, and with further diluting the zirconium alkoxide precursor with alcohol to the dilution ratio of 1:2 and 1:5, structural defects increased and a disordered structure was formed. At the same time, the center-to-center distance between the air spheres increased and the wall thickness of the macroporous structure decreased. Dilution in ethanol resulted in the formation of a less ordered structure, a larger pore diameter, and a thinner wall. It has been reported that, at higher dilution, the ethanol may have partially damaged the colloidal latex crystal, causing the decrease in order for the products.[26] In the present work, the well-ordered structures were

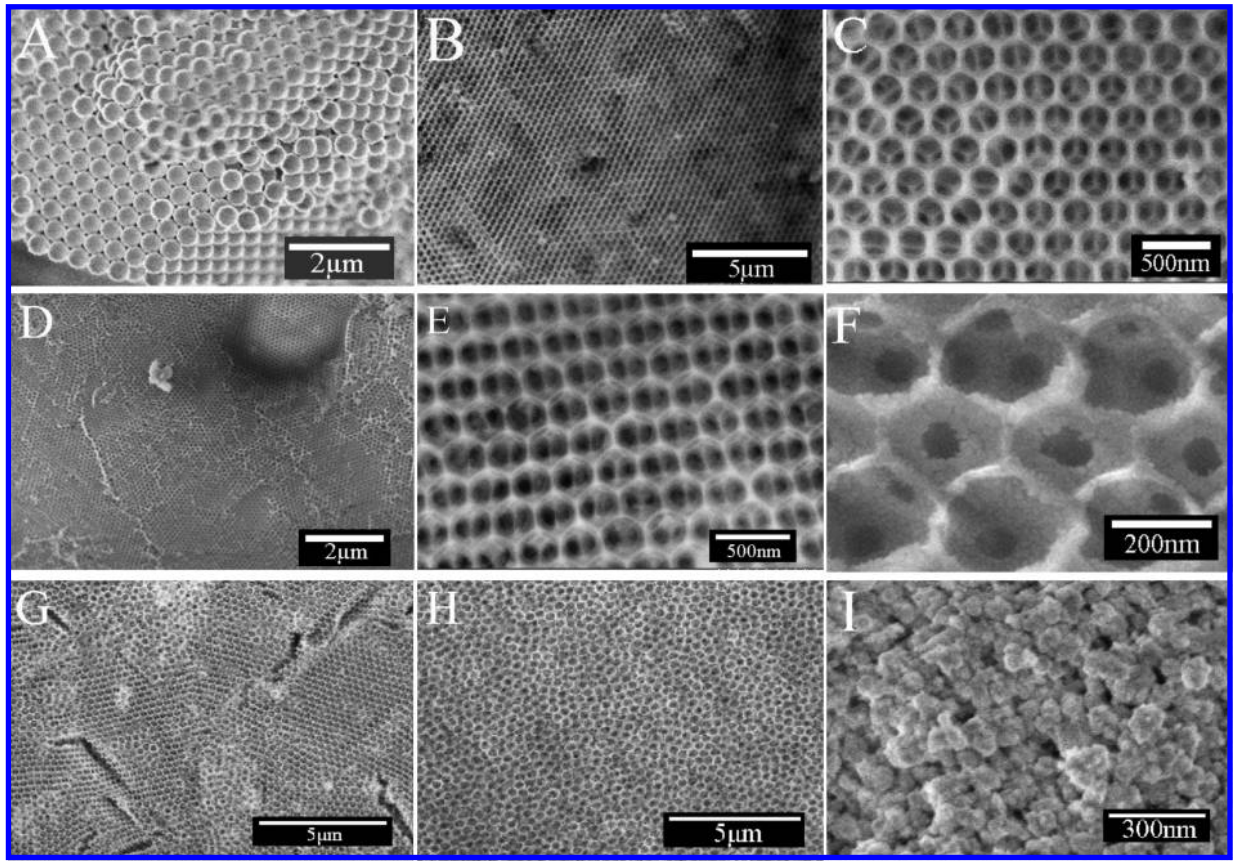

Figure 1. Field-emission SEM images of as-prepared (A) PS colloidal crystal, (B, C) PC1, (D−F) PC2, (G) 3DOM ZrO_2:Eu^{3+} with the dilution ratios of 1:2, (H) 3DOM ZrO_2:Eu^{3+} with the dilution ratios of 1:5, and (I) a crushed sample of PC1.

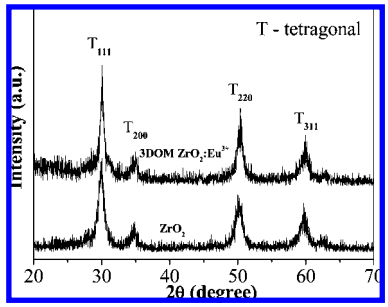

Figure 2. XRD patterns of 3DOM ZrO_2 and ZrO_2:Eu^{3+} composites.

obtained at the dilution ratio of 1:1 and the PC1 and PC2 were prepared at this dilution.

Figure 2 displays the XRD patterns of the 3DOM ZrO_2 and ZrO_2:Eu^{3+}. According to JCPDS standard cards, the two samples exhibit a tetragonal phase with the characteristic 2θ values at 30.1° (111), 35.2° (200), 50.4° (220), and 59.9° (311), respectively (JCPDS file 17-0923). On the basis of the Scherrer equation, the average crystalline size was estimated to be 12 nm, which is very consistent with the result of SEM images. Compared to the pure ZrO_2, no indication of any crystalline phase related to Eu_2O_3 appeared. This result definitely reveals that Eu^{3+} ions were probably dispersed into the ZrO_2 framework and substituted the Zr^{4+} ions in the lattice matrix. Because the radium of Zr^{4+} (0.089 nm) is quite close to that of Eu^{3+} (0.094 nm), it is hard to identify the variation of lattice constants according to XRD spectra even as Zr^{4+} ions are substituted by Eu^{3+} ions. If Eu^{3+} ions did not come into the lattices of ZrO_2, Eu^{3+} should exist in the Eu_2O_3 phase, which might adsorb on the surface of the nanoparticles. To identify this case, we compared the luminescence spectrum of the present ZrO_2:Eu^{3+} sample with that of Eu_2O_3, which demonstrated that excitation band of Eu_2O_3 was located at 282 nm, while that of ZrO_2:Eu^{3+} was located at 243 nm. This indicates that Eu^{3+} ions came into ZrO_2 lattices instead of adsorbing on the surface of nanoparticles in the form of Eu_2O_3. Due to the substitution of Eu^{3+} for Zr^{4+} some anion defects (oxygen vacancy ($V_O^{\bullet\bullet}$) would be caused in the host lattices to achieve the effect of charge compensation ($Eu_2O_3 \xrightarrow{2ZrO_2} 2Eu'_{Zr} + V_O^{\bullet\bullet} + 3O_O$). The local environment surrounding Eu^{3+} in ZrO_2 will be further discussed in section III.4.

III.2. Effect of the Photonic Stop Band on PL in 3DOM ZrO_2:Eu^{3+}. As is clearly seen in Figure 1, the materials exhibited the hexagonal arrangement of air spheres, which corresponds to the (111) surface of a fcc structure with high filling. Hence, an estimation of the position of the photonic stop band can be obtained by a modified version of Bragg's law, combined with Snell's law to account for the reduced angle with respect to the normal that light travels upon entering the inverse opal: [14,18]

$$\lambda = \frac{2d_{hkl}}{m}(\sqrt{n_{\text{eff}}^2 - \sin^2\theta} \quad (1)$$

where λ is the wavelength of the stop band minimum, d_{hkl} is the interplanar spacing, m is the order of Bragg diffraction, n_{eff} is the average refractive index of the material, and θ is the angle measured from the normal to the planes. Since the measurements were performed on powder, randomly oriented samples, the spectra display minima at the calculated value for normal incidence ($\theta =$

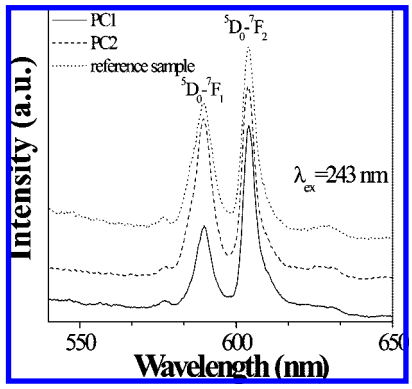

Figure 3. The emission spectra of PC1, PC2, and nonporous sample (λ_{ex} = 243 nm).

0°), and the angle-dependent term can be obtained from the equation

$$\lambda = \frac{2d_{hkl}}{m} n_{\text{eff}} = 1.633 D n_{\text{eff}} \quad (2)$$

The effective refractive index n_{eff} can be expressed as,

$$n_{\text{eff}} = n_{ZrO_2}\phi + n_{\text{air}}(1 - \phi) \quad (3)$$

where ϕ is the fractional volume of ZrO_2 (n = 2) and eq 3 gives $n_{\text{eff}} = 0.74 n_{\text{air}} + 0.26 n_{ZrO_2} = 1.26$. The center-to-center distances of the neighboring hollow spheres were measured to be 285 and 260 nm, respectively. According to eq 2, the stop band position for Bragg diffraction from (111) planes of PC1 and PC2 should occur at 586 and 535 nm, respectively.

In Figure 3, the emission spectra of PC1, PC2, and nonporous samples (as a reference sample) upon excitation into the charge transfer band (CTB) of Eu^{3+} at 243 nm were presented. It can be observed that the prominent emission bands appeared at 590 and 604 nm for all the samples, which are attributed to the $^5D_0$-$^7F_1$ and $^5D_0$-$^7F_2$ transitions of the Eu^{3+} ions and the ratios of $^5D_0$-$^7F_2$ to $^5D_0$-$^7F_1$ in PC1, PC2, and nonporous reference sample are 2.08, 1.20, and 1.40, respectively. As is well-known, the $^5D_0$-$^7F_2$ transition is electric-dipole allowed and its intensity is sensitive to the local structure surrounding the Eu^{3+} ions. However, the $^5D_0$-$^7F_1$ transition is magnetic-dipole allowed and its intensity shows very little variation with the crystal field strength acting on the Eu^{3+} ion. Therefore, the intensity ratio of $^5D_0$-$^7F_2$ to $^5D_0$-$^7F_1$ is closely related to the local environments surrounding Eu^{3+} for general nanocrystals.[27] Generally, the larger the intensity ratio of $^5D_0$-$^7F_2$ to $^5D_0$-$^7F_1$ is, the lower the local symmetry is.[28] Since the stop band of PC2 lies outside of the range of the emission band, the PL spectrum is unaffected by the 3D order and the smaller ratio of $^5D_0$-$^7F_2$ to $^5D_0$-$^7F_1$ compared with the reference sample was attributed to the change of local environments surrounding Eu^{3+} in the two kinds of materials. As have been studied in previous literature, the local environments surrounding the surface ions are different from those surrounding the inner ions.[29] In a nonporous reference sample, the number of atoms/ions locate at or near the surfaces of the particles is more than that of the 3D order sample, making the site symmetry of Eu^{3+} ions lower. As a consequence, the emission of $^5D_0$-$^7F_2$ in the reference sample is a little bit stronger than that in PC2. However, for the PC1 with a stop band at 586 nm, the emission for $^5D_0$-$^7F_1$ peaking at 590 nm was suppressed significantly. The PC1 and PC2 were fabricated under the same conditions, with the same 3D order structure; we consider that photonic crystal effects are responsible for the difference in the PL spectra of the two samples. An inhibition of the light emission from the ZrO_2:Eu^{3+} has occurred due to the influence of Bragg diffraction in the PC1 sample.

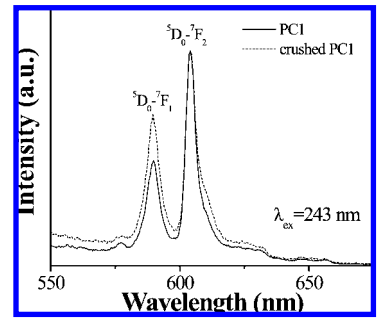

Figure 4. The emission spectra of PC1 and its corresponding crushed samples (λ_{ex} = 243 nm).

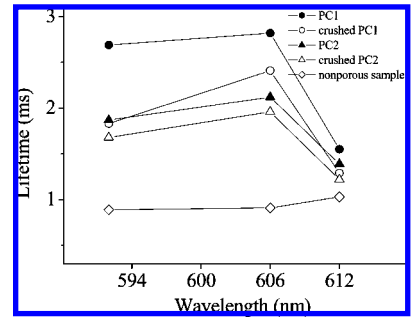

Figure 5. The graph of $^5D_0$-^7F_J (J = 1 and 2) luminescent lifetime as a function of the emission wavelength (592, 606, and 612 nm) in different samples.

To further investigate the influence of the photonic stop band of ZrO_2:Eu^{3+} on its PL emission spectrum, as-prepared PC1 sample was directly ground to destroy the regular 3D order. Figure 1H shows the SEM image of the crushed PC1 sample. The emission spectra of original 3D order and crushed ZrO_2:Eu^{3+}samples are shown in Figure 4. As discussed above, the Eu^{3+} ions in the crushed sample have lower local symmetry, which should make the $^5D_0$-$^7F_2$ became stronger in comparison with that in the 3D order sample. However, as shown in Figure 4, the intensity ratio of $^5D_0$-$^7F_2$ to $^5D_0$-$^7F_1$ in crushed PC1 sample decreased from 2.08 to 1.41 compared with that of PC1. The $^5D_0$-$^7F_2$ became relatively weak when the framework was crumbled. It is suggested that the relative change did not come form the local structure surrounding the Eu^{3+} ions, but from the photonic crystal structure, which was responsible for the depression observed in the PL emission spectrum of $^5D_0$-$^7F_1$ in PC1.

III.3. PL Decay Dynamics. The room temperature luminescent dynamics were also measured. The dependence of $^5D_0$-^7F_J luminescent lifetime on emission wavelength (592, 606, and 612 nm) in different samples is presented in Figure 5. It is obvious that the fluorescence lifetime depended not only on the sample, but also on the emission wavelength. As shown in Figure 5, the general features can be concluded as follows: (1) In the nonporous sample, the lifetime of the $^5D_0$-^7F_J transitions had only a little variation at different wavelengths. (2) In the PC1, PC2, and the corresponding crushed samples, the lifetime depended strongly on detected wavelength. The lifetime at 612 nm was obviously shorter than that at 606 and 592 nm. (3) In comparison to the nonporous sample, the lifetime of $^5D_0$-^7F_J in

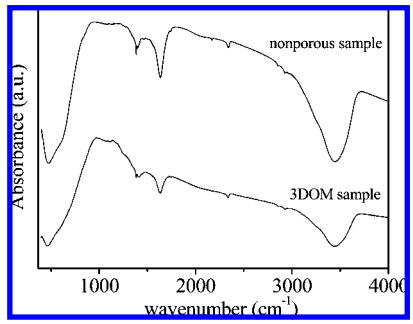

Figure 6. FTIR spectra of as-prepared 3DOM ZrO_2:Eu^{3+} and the nonporous materials.

the PC1, PC2, and the corresponding crushed PC1 and PC2 increased to different contents. (4) The lifetime in the crushed PC1 sample was apparently shorter than that of PC1 when monitoring at 592 nm, while the lifetime in the crushed PC2 had only a little decrease in comparison to that of PC2.

Now let us explain the above facts in turn. Features 1 and 2 can be attributed to different local environments surrounding Eu^{3+} in different samples. In the nonporous sample, there existed only one symmetry site for the $^5D_0$-^7F_J transition of Eu^{3+}, while there existed three different symmetry sites of Eu^{3+} in the 3DOM samples (this will be proved by the site-selective excitation experiments in the next section). The Eu^{3+} ions locating at different sites should have different lifetimes. After the 3DOM samples were crushed, the symmetry sites did not change. Feature 3 can be attributed to the decrease of nonradiative relaxation rate of Eu^{3+} in the 3DOM samples. In the nanocrystals, a large number of surface adsorptions such as OH^- and CO_3^{2-} bonds are generally involved. These bonds have large phonon energy and act as nonradiative relaxation channels, leading the nonradiative transition rate to increase.

Figure 6 shows the FTIR spectra of the nonporous and the 3DOM ZrO_2:Eu^{3+}. In Figure 6, the 3DOM and nonporous samples both exhibit four peaks in the measured range, locating at 470, 1380, 1635, and 3450 cm^{-1}, respectively. The 470 cm^{-1} band is assigned to the Zr−O vibration and the 1380 cm^{-1} band can be attributed to very small amounts of *n*-BuOH originating from the resource of Zr.[30] The bands located at 1635 and 3450 cm^{-1} are assigned to the −OH bending and stretching modes, respectively, corresponding to the surface contamination of water. It is obvious that the surface adsorption of water in the 3DOM sample became much less in contrast to that in the nonporous sample, thus the nonradiative relaxation rate decreased and the lifetime became longer. Here, we believe that the surface contamination was easily removed compared with the nonporous sample due to the process of combustion and decomposition of PS templates. Meanwhile, due to the void volume available to exhale, macroporous structure made the calcinations more effective.

As to feature 4, we consider that it is still related to the change of radiative decay rate in photonic crystal structure. According to Fermi's golden rule, the radiative decay rate (inverse lifetime) is proportional to the projected local radiative density of optical states (DOS), to which the emitters couple.[31,32] In ideal photonic crystals, the local DOS and hence the decay rate ideally vanish over a frequency range known as the PBG.[15] Due to the $^5D_0$-$^7F_1$ emission of Eu^{3+} in the calculated photonic stop band in the case of PC1, vacuum fluctuations are expelled from the crystal and the spontaneous decay is inhibited and leads to the increase of fluorescence lifetime. As the PC1 was crushed, the photon crystal structure disappeared, and thus the lifetime

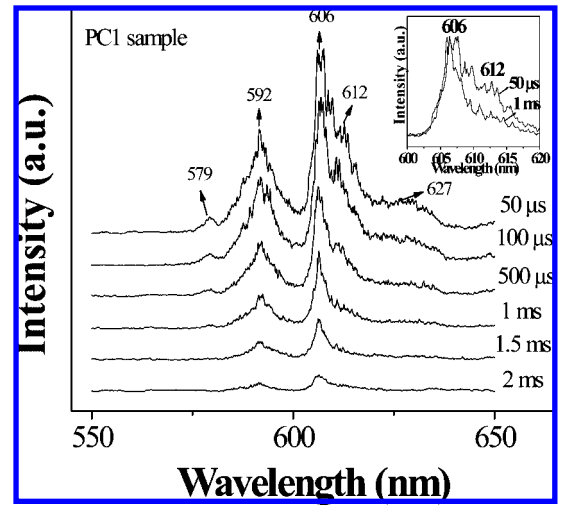

Figure 7. The time-resolved emission spectra of PC1 measured at 13 K (λ_{ex} = 266 nm). The inset is a comparison of normalized emission spectra when the delay times are 50 μs and 1 ms.

decreased again. In unperfected photonic crystals, the radiative lifetime was usually observed to increase in the photonic stop band region due to the decrease of DOS.[9,15−19] Photonic crystals have been demonstrated as an effective way of controlling the radiative lifetime.

III.4. Symmetry Sites in Different Samples. To understand the local environments surrounding Eu^{3+} in different samples, the time-resolved emission spectra and site-selective excitation experiments were performed. Figure 7 shows the time-resolved emission spectra of PC2 (measured at 13 K). In the emission spectra, one $^5D_0$-$^7F_0$ line at 579 nm, one $^5D_1$-$^7F_1$ line at 592 nm, and three Stark $^5D_0$-$^7F_2$ lines at 606, 612, and 627 nm were identified. As the delay time increased in the studied range, the intensity of the peak located at 612 nm decreased dramatically and nearly disappeared as the delay time increased to 1 ms (inset of Figure 7), while the peak positioned at 592 and 606 nm decreased slowly, indicating that the lifetime at 612 nm was shorter than that at 592 and 606 nm and was on the order of 1 ms, which is very consistent with the results listed in Figure 5. Note that in the nonporous sample, the lifetime changed only a little as monitored at the same wavelengths. This indicates that different local environments surrounding Eu^{3+} between 3DOM and the nonporous sample may exist. To determine this point, the site-selective excitation experiments were performed. Figure 8 shows the $^5D_0$-$^7F_0$ site-selective excitation spectra monitoring different $^5D_0$-$^7F_2$ sites (left) and the $^5D_0$-$^7F_2$ emission spectra selectively exciting $^5D_0$-^7F transitions$_0$ (right) in 3DOM sample in contrast to the nonoporous sample. As shown in Figure 8A (left), in the nonporous sample, there is only one excitation peak located at 578.69 nm (site A) appeared, and the shape and location of the peak had only a little variation when monitored at different wavelengths, implying that only one symmetry existed. With excition at different wavelengths (right), the intensity ratios of the 606 to 612 nm peak had only a little change. This could be attributed to slightly different local environments among the luminescent Eu^{3+} ions. In PC1(see Figure 8B), two new excitation peaks were identified by monitoring the 606 nm peak, located at 577.1 (site B) and 579.76 nm (site C). This implies that three luminescent symmetry sites existed in the 3DOM materials. The existence of extra symmetry sites in the 3DOM ZrO_2 could be attributed to the special preparation method, despite not being able to determine the detailed origin at present. On the basis of the results of lifetime

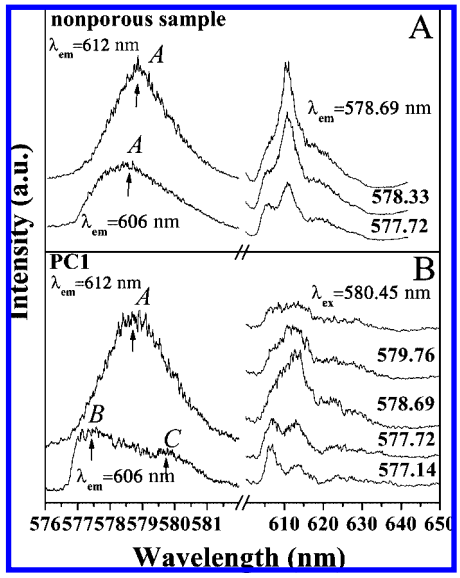

Figure 8. Site-selective excitation (left) and emission spectra (right) of the PC1 sample and nonporous sample.

constants and the site-selective excitation experiments, we can conclude that the lifetime for Eu^{3+} ions locating at sites B and C is longer than that at site A and thus leads to the lifetime of Eu^{3+} at 606 nm being longer.

IV. Conclusions

In summary, two different pore size air sphere 3DOM ZrO_2:Eu^{3+} inverse opal materials were successfully designed and prepared by using the sol−gel method and the templating technology. Their PL properties, local environment, and the effect of the photonic band gap on the spontaneous emission of Eu^{3+} were studied by contrast to the nonporous and crushed samples. In the PC1 sample, due to the influence of the photonic band (∼586 nm) effect, a significant suppression of the $^5D_0$-$^7F_1$ emission and an increase of the luminescence lifetime were observed. In the crushed PC1, the suppression of emission was restored due to the disappearance of the photonic band gap. In the 3DOM samples, two new symmetry sites for the emissions of Eu^{3+}were identified by site-selective excitation spectra. Due to the existence of different sites, the lifetime of $^5D_0$-^7F_J depended strongly on the emission wavelength.

Acknowledgment. This work is supported by the financial support of Nation Natural Science Foundation of China (Grant Nos. 50772042, 10704073, and 10504030) and the 863 Project of China (2007AA032314).

References and Notes

(1) Yablonovitch, E. *Phys. Rev. Lett.* **1987**, *58*, 2059.
(2) John, S. *Phys. Rev. Lett.* **1987**, *58*, 2486.
(3) Romanov, S. G.; Fokin, A. V.; De La Rue, R. M. *Appl. Phys. Lett.* **1999**, *74*, 1821.
(4) Lin, S. Y.; Fleming, J. G.; Hetherington, D. L.; Smith, B. K.; Biswas, R.; Ho, K. M.; Sigalas, M. M.; Zubrzycki, W.; Kurtz, S. R.; Bur, J. *Nature* **1998**, *394*, 251.
(5) Joannopoulos, J. D.; Villeneuve, P. R.; Fan, S. H. *Nature* **1997**, *386*, 143.
(6) Finlayson, C. E.; Ginger, D. S.; Greenham, N. C. *Chem. Phys. Lett.* **2001**, *338*, 83.
(7) Zhang, J.; Fu, Y.; Lakowicz, J. R. *Anal. Biochem.* **2007**, *360*, 266.
(8) Li, Y. Z.; Kunitake, T.; Fujikawa, S.; Ozasa, K. *Langmuir* **2007**, *23*, 9109.
(9) Nikolaev, I. S.; Lodahl, P.; Vos, W. L. *J. Phys. Chem. C* **2008**, *112*, 7250.
(10) Petrov, E. P.; Bogomolov, V. N.; Kalosha, I. I.; Gaponenko, S. V. *Phys. Rev. Lett.* **1998**, *81*, 77.
(11) Romanov, S. G.; Fokin, A. V.; De La Rue, R. M. *Appl. Phys. Lett.* **2000**, *76*, 1656.
(12) Tsvetkov, M. Y.; Kleshcheva, S. M.; Samoilovich, M. I.; Gaponenko, N. V.; Shushunov, A. N. *Microelectron. Eng.* **2005**, *81*, 273.
(13) Kalkman, J.; de Bres, E.; Polman, A.; Jun, Y.; Norris, D. J.; Hart, D. C.; Hoogenboom, J. P.; van Blaaderen, A. *J. Appl. Phys.* **2004**, *95*, 2297.
(14) Aloshyna, M.; Sivakumar, S.; Venkataramanan, M.; Brolo, A. G.; Veggel, V. *J. Phys Chem C* **2007**, *111*, 4047.
(15) Lodahl, P.; van Driel, A. F.; Nikolaev, I. S.; Irman, A.; Overgaag, K.; Vanmaekelbergh, D. L.; Vos, W. L. *Nature* **2004**, *430*, 654.
(16) Zhou, J.; Zhou, Y.; Buddhudu, S.; Ng, S. L.; Lam, Y. L.; Kam, C. H. *Appl. Phys. Lett.* **2000**, *76*, 3513.
(17) Li, B.; Zhou, J.; Zong, R. L.; Fu, M.; Li, L. T. *J. Am. Ceram. Soc.* **2006**, *89*, 2308.
(18) Yang, Z.; Zhou, J.; Huang, X.; Yang, G.; Xie, Q.; Sun, L.; Li, B.; Li, L. *Chem. Phys. Lett.* **2008**, *455*, 55.
(19) Jeon, S.; Braun, P. V. *Chem. Mater.* **2003**, *15*, 1256.
(20) Dai, Q.; Song, H. W.; Pan, G. H.; Bai, X.; Zhang, H.; Qin, R.; Hu, L.; Zhao, H.; Lu, S.; Ren, X. *J. Appl. Phys.* **2007**, *102*, 054311.
(21) Pan, G.; Song, H. W.; Bai, X.; Liu, Z.; Yu, H.; Di, W.; Li, S.; Fan, L.; Ren, X.; Lu, S. *Chem. Mater.* **2006**, *18*, 4526.
(22) Peng, H.; Song, H.; Chen, B.; Lu, S.; Huang, S. *Chem. Phys. Lett.* **2003**, *370*, 485.
(23) Chen, G.; Somesfalean, G.; Liu, Y.; Zhang, Z.; Sun, Q.; Wang, F. *Phys. Rev. B* **2007**, *75*, 195204.
(24) Patra, A.; Friend, C. S.; Kapoor, R.; Prasad, P. N. *J. Phys. Chem. B* **2002**, *106*, 1909.
(25) De la Rosaa, E.; Salas, P.; Desirena, H.; Angeles, C.; Rodríguez, R. A. *Appl. Phys. Lett.* **2005**, *87*, 241912.
(26) Holland, B. T.; Blanford, C. F.; Do, T.; Stein, A. *Chem. Mater.* **1999**, *11*, 795.
(27) Wu, C.; Qin, W.; Qin, G.; Zhao, D.; Zhang, J.; Huang, S. *Appl. Phys. Lett.* **2003**, *82*, 520.
(28) Yu, L.; Song, H.; Lu, S.; Liu, Z.; Yang, L.; Kong, X. *J. Phys. Chem. B* **2004**, *108*, 16697.
(29) Peng, H.; Song, H.; Chen, B.; Lu, S.; Huang, S. *Chem. Phys. Lett.* **2003**, *370*, 485.
(30) Gedanken, A.; Reisfeld, R.; Sominski, E.; Palchik, O.; Koltypin, Y.; Panczer, G.; Gaft, M.; Minti, H. *J. Phys. Chem. B* **2000**, *104*, 7057.
(31) Sprik, R.; van Tiggelen, B. A.; Lagendijk, A. *Europhys. Lett.* **1996**, *35*, 265.
(32) Vats, N.; John, S.; Busch, K. *Phys. Rev. A* **2002**, *65*, 043808.

JP8075063